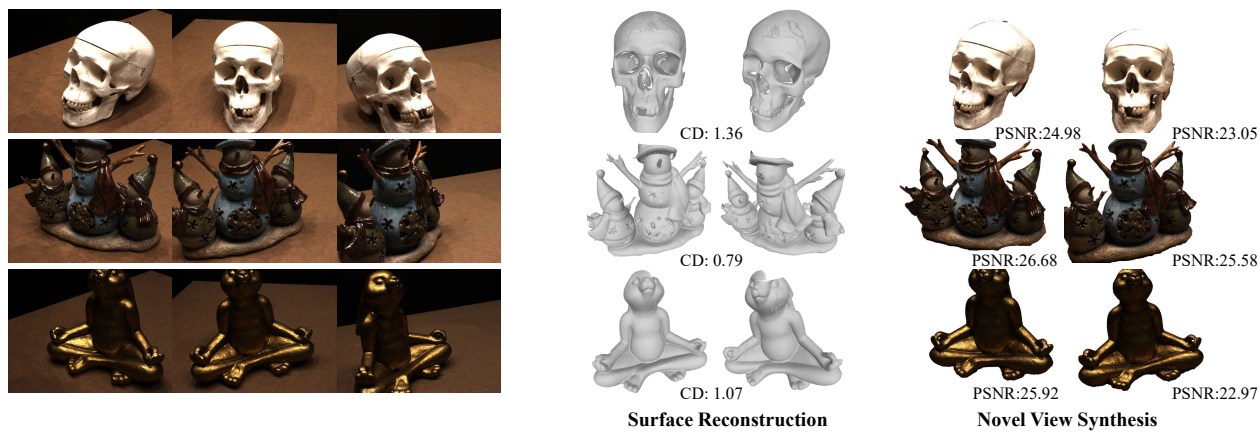


SolidGS: Consolidating Gaussian Surfel Splatting for Sparse-View Surface Reconstruction

Zhuowen Shen^{1,2*} Yuan Liu^{3,4} Zhang Chen² Zhong Li² Jiepeng Wang⁵ Yongqing Liang¹
 Zhengming Yu¹ Jingdong Zhang¹ Yi Xu² Scott Schaefer¹ Xin Li¹ Wenping Wang¹
¹Texas A&M University ²OPPO US Research Center ³Nanyang Technological University
⁴Hong Kong University of Science and Technology ⁵The University of Hong Kong



Input: 3 Training Views

Output: Explicit SolidGS

Figure 1. **Overview of SolidGS.** We present SolidGS, which reconstructs a consolidated Gaussian field from sparse inputs. Given only three input views, our approach enables high-precision and detailed mesh extraction, and high-quality novel view synthesis, achieved within just three minutes.

Abstract

Gaussian splatting has achieved impressive improvements for both novel-view synthesis and surface reconstruction from multi-view images. However, current methods still struggle to reconstruct high-quality surfaces from only sparse view input images using Gaussian splatting. In this paper, we propose a novel method called SolidGS to address this problem. We observed that the reconstructed geometry can be severely inconsistent across multi-views, due to the property of Gaussian function in geometry rendering. This motivates us to consolidate all Gaussians by adopting a more solid kernel function, which effectively improves the surface reconstruction quality. With the additional help of geometrical regularization and monocular normal estimation, our method achieves superior performance on the sparse view surface reconstruction than all the Gaussian splatting methods and neural field methods on the widely used DTU, Tanks-and-Temples, and LLFF datasets.

1. Introduction

Accurately reconstructing the geometry while maintaining photo-realistic novel view synthesis results has always been a popular topic in the field of 3D computer vision [40]. Previously, many works [24, 46, 53] built on Neural Radiance Field (NeRF) [32] incorporating Signed Distance Function (SDF) have achieved remarkable reconstruction results. However, these neural representation methods usually suffer from hours of training time, and rendering an image is usually inefficient for real-time applications such as AR and VR.

Recently, 3D Gaussian Splatting (3DGS) [21] adopts an explicit point-based representation and achieves minutes-long training with comparable NVS quality. The succeeding works [7, 18, 58] extend 3DGS to reconstruct high-quality surfaces, achieving comparable results to NeRF-based methods. The key idea of these explicit methods [18, 50] is to squash Gaussian primitives to approximate surfaces and explicitly calculate the exact intersection points between the camera rays and Gaussian primitives in the rendering. With the exact intersections, these works can render high-quality normal and depth maps from the Gaus-

*Work partially done during his internship at OPPO US Research Center.

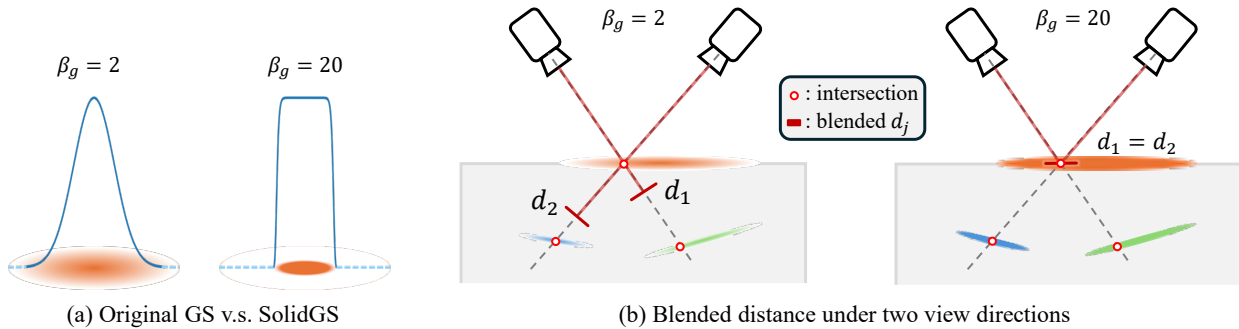


Figure 2. **Illustration of SolidGS.** (a) The Gaussian functions \mathcal{G}_i of the original 3DGS and SolidGS in Eq. (6). (b) Visualization of ray-plane intersections and blended depths $d_j, j \in \{1, 2\}$ for two types of Gaussians. In the original Gaussian, as rays deviate from the Gaussian center, the depth is blended with the background Gaussians, leading to inconsistent multi-view geometry in 3D space. Meanwhile, our SolidGS is opaque in most of its effective areas, giving out consistent geometry regardless of view directions.

sians and constrain the surface by applying geometry regularization. Though the aforementioned works made tremendous progress in multi-view surface reconstruction, these methods usually require hundreds of multi-view images as input. In many applications such as AR/VR or robotics, we only have access to sparse views and these methods struggle to reconstruct reasonable surfaces from these sparse view images.

We find that the main reasons for the degraded reconstruction quality are the multi-view depth inconsistency and insufficient supervision from sparse input. As shown in Fig. 2, though existing methods try to squash the Gaussian primitives into planes, a strong depth inconsistency still exists. Due to the property of the Gaussian function during alpha blending, the opacity of a Gaussian primitive unavoidably decreases as deviating from its center, which causes different rendered depth values for two different rays that intersect at the same point on the surface. Consequently, the inconsistent depth causes noisy reconstructed surfaces in existing methods [7, 18]. Meanwhile, the sparse view inputs fail to provide enough constraints for the Gaussian opacity to converge to solid surfaces, which further degrades the reconstruction quality.

In this paper, we propose a novel method, SolidGS, to tackle the above challenges for sparse-view surface reconstruction. The key ideas of our method are consolidating the Gaussians and introducing additional geometry constraints. These constraints consist of self-supervision geometry loss from virtual views and monocular normal regularization. Both the consolidation of Gaussians and the proposed constraints greatly improve the surface reconstruction quality within the sparse view setting.

As shown in Fig. 2 (b), consolidating the Gaussian primitives into our SolidGS prevents camera rays from penetrating the Gaussian primitives, thereby substantially reducing the rendered depth inconsistency and enhancing reconstruction quality. A naive way for such consolidation is to directly apply a constant opacity value for the primitive to replace the Gaussian function. However, this method poses

challenges for stable optimization, as it causes differentiability issues over the primitives [27, 37]. To promote stable optimization while consolidating Gaussian primitives, we get inspiration from GES [16] to adopt a trainable exponential factor within the Gaussian function and encourage the exponential factor to converge to a large value by sharing the factor for all Gaussian primitives. This strategy enables our representation to be a vanilla Gaussian representation in the beginning while gradually stabilizing into solid primitives throughout the optimization process.

In addition to consolidating Gaussian primitives, we incorporate several novel constraints to guide our optimization process toward accurate surface reconstruction. Specifically, we introduce additional self-supervised geometry regularization from virtual cameras. We also estimate normal maps from input views using monocular normal estimators [17]. These virtual view regularizations and normal maps stabilize the optimization and lead to accurate surface reconstruction.

We have conducted extensive experiments on the DTU [20], Tanks and Temples [22], and LLFF [31] dataset. The results show that our method reconstructs high-quality surfaces even only given 3 input RGB images in 3 minutes, which greatly improves the reconstruction quality than Gaussian splatting-based methods [23, 50] while being much more efficient than previous neural SDF-based baselines [19, 29].

In summary, our major contributions are threefold:

- We propose SolidGS, a novel representation that consolidates the opacity of Gaussians by introducing a shared, learnable solidness factor, enabling multi-view consistent geometry rendering.
- We introduce a new framework with geometric constraints to train our SolidGS representation, which consists of geometric priors and regularizations.
- We perform extensive experiments on DTU, Tanks and Temples, and LLFF datasets. Our method outperforms existing state-of-the-art methods on these datasets.

2. Related works

2.1. Neural Volume Rendering

Neural volume rendering uses neural networks to represent 3D scenes as continuous volumetric data for realistic, view-dependent rendering, which was first introduced in Neural Volume [28]. It surpasses traditional methods by producing seamless, photorealistic views and is essential for applications like VR and 3D graphics. A pivotal development was the introduction of Neural Radiance Fields (NeRF) [32]. NeRF employed a differentiable volumetric rendering technique to reconstruct a neural scene representation, achieving impressive photorealistic view synthesis with view-dependent effects. To accelerate its optimization, subsequent research replaces the neural scene representation with explicit or hybrid scene representations, such as voxel grids [13, 43], low-rank tensors [6], tri-planes [3], multi-resolution hash grids [33], and even point pivoted radiance field [49]. Recently, 3D Gaussian Splatting (3DGS) [21] demonstrates the possibility of 3D Gaussians modeling continuous distributions of color and opacity across space, significantly enhancing rendering speed and reducing memory consumption. More succeeding works [26, 36, 57] continue to refine the visual quality. To further exploit the power of Gaussian Splatting, our work focuses on a more challenging but practical sparse-view setting.

2.2. Novel View Synthesis from Sparse View

Sparse-view Novel View Synthesis (NVS), which focuses on rendering high-quality images from limited camera perspectives, has garnered extensive research interest in recent years. NeRF-based methods improve sparse-view reconstruction by leveraging additional constraints [34, 41, 51], multi-view stereo priors [5], and depth priors [11, 39, 44]. While these methods perform optimization for the individual scene, there are also works that directly reconstruct the scene in a feed-forward manner [12, 42, 55]. However, these works still suffer from heavy volume sampling and long training time. Gaussian-based techniques have emerged as an efficient solution. Many works have engaged in-depth recently [1, 35, 48, 60]. DNGaussian [23] leveraging depth regularization for efficient and high-quality few-shot NVS. MVPGS [50] extends this approach by integrating multi-view priors to improve geometry consistency across views, thereby enhancing performance in sparse-view settings. Gaussian-based feed-forward methods also achieve superior quality [4, 8]. Our primary target is to reconstruct multi-view consistent geometry.

2.3. Surface Reconstruction from Sparse View

Accurately reconstructing geometry simultaneously during neural volume rendering has gained significant interest recently. NeuS [46] and VolSDF [53] learn SDF during ra-

diance field training to achieve accurate geometry reconstruction. More works [14, 25, 45] improve the geometry quality further. To achieve accurate geometry reconstruction from sparse view inputs [19, 29, 38, 47, 54], SparseNeus [29] learns generalizable priors from image features for sparse view reconstruction. Neusurf [19] leverages on-surface priors obtained from SfM to achieve faithful surface reconstruction. More recently, SparseCraft [54] regularized the model with learning-free multi-view stereo (MVS) cues without pretrained priors. Although the reconstruction quality has been improved, these methods are still slow in training due to the property of volume rendering. With the recent development of 3D Gaussian Splatting [21], SuGaR [15] proposed a method to extract Mesh from 3DGS. 2DGS [18] achieves view-consistent geometry by collapsing the 3D volume into a set of 2D oriented planar Gaussian disks. GOF [58] establishes a Gaussian opacity field, enabling geometry extraction by directly identifying its level-set. PGSR [7] improves the quality further by utilizing the MVS priors. However, these methods require dense multi-view inputs to get accurate reconstructed results. To tackle this, we use solid Gaussian Surfels as a representation to achieve fast and accurate geometry reconstruction from sparse views.

3. Method

Given sparse view inputs (e.g. 3 views), our goal is to reconstruct the surface of the scene with high accuracy and precision while maintaining a satisfactory novel view synthesis result simultaneously. An overview of our method is provided in Fig. 3. In this section, we first review the 3D Gaussian Splatting [21] in Sec. 3.1.1 and introduce our modified Gaussian representation, SolidGS, in Sec. 3.1.2. To guide the Gaussians to be solid and 3D consistent, we add the geometric regularization in Sec. 3.2.1 alongside geometric clues from the monocular normal estimator in Sec. 3.2.2.

3.1. SolidGS

3.1.1. 3D Gaussian Splatting Preliminary

3D Gaussian Splatting [21] utilizes a set of explicit 3D Gaussians $\{\mathcal{G}_i\}$ to represent a 3D scene. Each Gaussian is parameterized by an opacity (ρ_i), a center location ($\boldsymbol{\mu}_i \in \mathbb{R}^3$), a color ($c_i \in \mathbb{R}^3$), a rotation ($r_i \in \mathbb{R}^4$) in quaternion form, and a scale vector ($s_i \in \mathbb{R}^3$). In the world coordinate, the Gaussian distribution is defined as:

$$\mathcal{G}_i(\mathbf{x}) = \exp \left\{ -\frac{1}{2} ((\mathbf{x} - \boldsymbol{\mu})^\top \boldsymbol{\Sigma}^{-1} (\mathbf{x} - \boldsymbol{\mu})) \right\}, \quad (1)$$

where $\boldsymbol{\Sigma}_i \in \mathbb{R}^{3 \times 3}$ is the corresponding 3D covariance matrix. The covariance matrix $\boldsymbol{\Sigma}_i$ can be factorized by $\boldsymbol{\Sigma}_i = R_i S_i S_i^\top R_i^\top$ into a scaling matrix $S_i \in \mathbb{R}^{3 \times 3}$ and a rotation matrix $R_i \in \mathbb{R}^{3 \times 3}$.

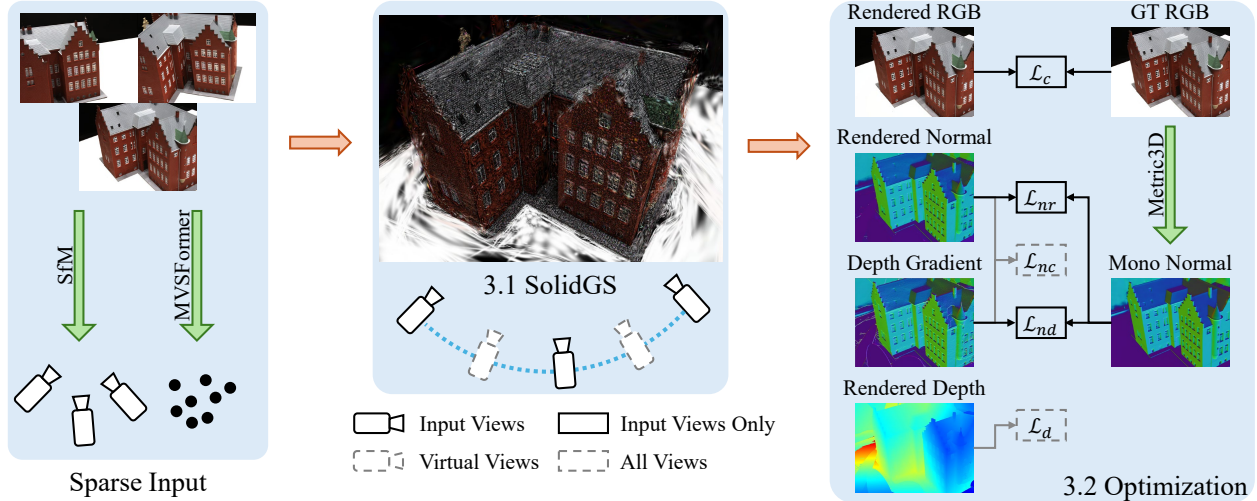


Figure 3. **SolidGS Framework.** With 3 input views, we initialize the camera pose with COLMAP and the point clouds with MVFormer. Virtual views are generated by linear interpolation between pairs of training views to provide additional geometric regularization. We represent the scene with our SolidGS and gradually enhance the solidity during training. SolidGS are optimized with photometric loss, monocular normal loss, and geometric regularization (normal consistency loss and depth distortion loss).

3DGS enables fast rendering by α -blending. The color $C \in \mathbb{R}^3$ of a pixel x can be obtained through α -blending:

$$C = \sum_{i \in N} T_i \alpha_i c_i, \quad T_i = \prod_{j=1}^{i-1} (1 - \alpha_j), \quad (2)$$

where $\alpha_i = \rho_i \mathcal{G}_i(x)$ is the blending weight. T_i is the cumulative transmittance, and N is the number of Gaussians that the ray passes through.

For geometry rendering, we use the flattened 3DGS in PGSR [7], and calculate the distance from the plane to the camera center:

$$d_i = (\boldsymbol{\mu}_i - T_c) \cdot \mathbf{n}_i, \quad (3)$$

where T_c is the camera center and \mathbf{n}_i is the normal direction corresponding to the minimum scale factor of the Gaussian.

Normal and distance maps are rendered with α -blending:

$$\mathbf{N} = \sum_{i \in N} T_i \alpha_i \mathbf{n}_i, \quad D = \sum_{i \in N} T_i \alpha_i d_i. \quad (4)$$

Then, the depth map is acquired by intersecting rays with the plane:

$$\mathbf{D}(p) = \frac{D}{\mathbf{N}(p)K^{-1}[p, 1]}, \quad (5)$$

where $p = [u, v]^\top$ is the 2D position on the image plane and K is the intrinsic matrix of the camera.

3.1.2. Solid Gaussian Representation

In the original Gaussian splatting, an outstanding issue for geometry rendering is the non-solid nature of Gaussian primitives. As shown in Fig. 2 (a), the alpha value of the intersection point decreases quickly as it deviates from the Gaussian center. Therefore, during α -blending, rendered depth could be inconsistent for two rays intersecting the

same 3D Gaussian, as shown in Fig. 2 (b). This inconsistency would introduce extra difficulties during optimization and lead to degraded surface reconstruction quality.

To fix this issue, we need to increase the solidity of Gaussians. We substitute the Gaussian distribution in Eq. (1) with the generalized exponential Gaussian distribution:

$$\mathcal{G}_i(\mathbf{x}) = \exp \left\{ -\frac{1}{2} \left((\mathbf{x} - \boldsymbol{\mu})^\top \boldsymbol{\Sigma}^{-1} (\mathbf{x} - \boldsymbol{\mu}) \right)^{\frac{\beta_i}{2}} \right\}, \quad (6)$$

which was first introduced in GES [16] for fast rendering and memory efficiency. β_i is a learnable parameter to control the individual Gaussian density distribution and effective region. In our SolidGS, we use a global shared solidity factor β_g for all Gaussians. This way, we can better control the solidity of all Gaussians and make them grow solid during the training.

As training proceeds, β_g automatically grows larger. As shown in Fig. 2 (a), the distribution approximates the uniform distribution and the Gaussian consolidates between $(\boldsymbol{\mu} - \boldsymbol{\sigma}, \boldsymbol{\mu} + \boldsymbol{\sigma})$. In Fig. 2 (b), when $\beta_g = 20$, the Gaussian already has unified alpha blending weight α_i over most of its effective area. The distance rendered would be identical regardless of the view directions on the Gaussian. This consistent geometry rendering would stabilize the optimization and consequently promote the final surface reconstruction.

3.2. Optimizations

3D Gaussian splatting [21] employs an RGB reconstruction loss, \mathcal{L}_c , combining \mathcal{L}_1 and D-SSIM terms between rendered and ground truth images, to encourage realistic image synthesis. However, with sparse-view inputs, this loss is not sufficient to form a consistent 3D geometry. To address this, we introduce additional geometric regularization

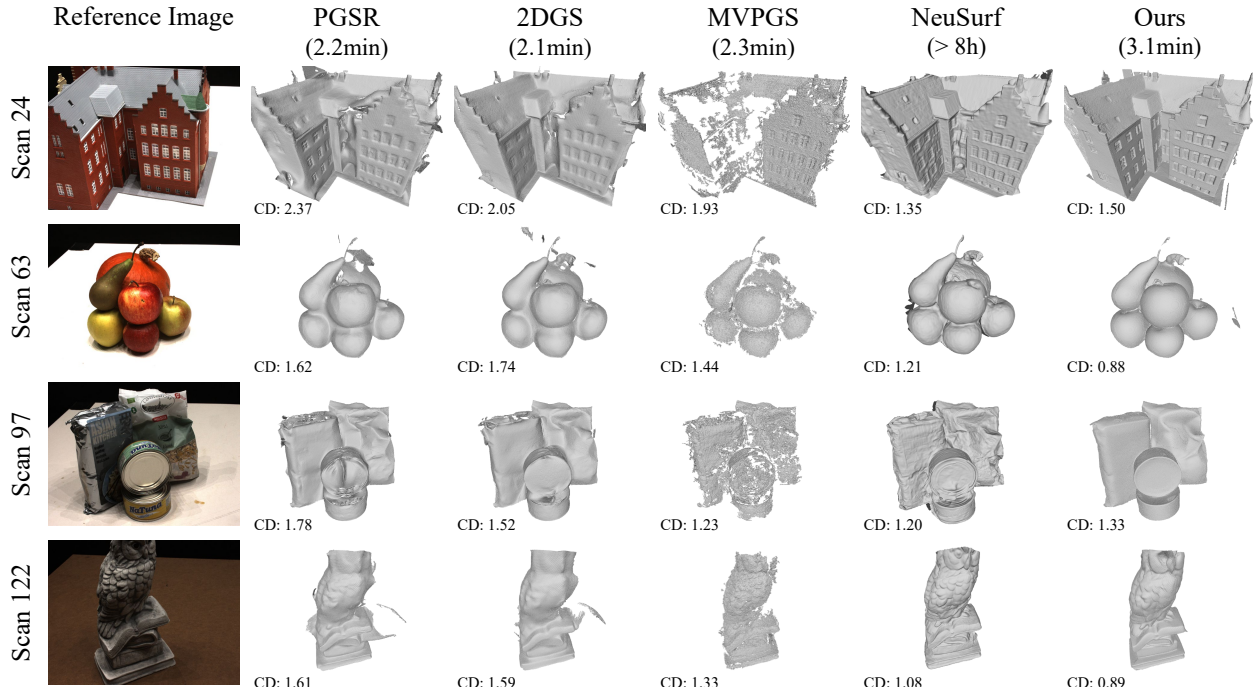


Figure 4. **Qualitative Mesh Results on DTU Dataset.** We show the reconstructed meshes with the closest input view for reference. Meshes are fused using the TSDF + Marching Cube method for explicit methods including PGSR [7], 2DGS [18], MVPGS [50], and our method. NeuSurf [19] maintains an SDF, from which the mesh is extracted using the Marching Cube.

to better guide Gaussian rotations and positions. We also recognized the limited constraints that sparse views impose on surface quality. We incorporate monocular normal priors from visual foundation models to enhance geometric accuracy. We put all optimization terms in Fig. 3.

3.2.1. Geometric Regularizations

Normal consistency loss. Following [7, 18, 58], the normal consistency loss \mathcal{L}_{nc} measures the consistency between the directly rendered normal and the normal calculated from the depth map,

$$\mathcal{L}_{nc} = \sum_i \alpha_i (1 - \mathbf{n}_i^\top \mathbf{N}_i), \quad (7)$$

where i is the index of the pixel, and \mathbf{n}_i represents the normal calculated from the gradient of the depth map. This loss ensures local smoothness of the rendered depth.

Depth distortion loss. We also use the depth distortion loss \mathcal{L}_d in [18, 58], which penalizes variations in depth among Gaussians on the same ray and reduces depth inconsistency,

$$\mathcal{L}_d = \sum_{i,j} \alpha_i \alpha_j |\mathbf{D}(p)_i - \mathbf{D}(p)_j|, \quad (8)$$

where $\alpha_i = \rho_i \mathcal{G}_i(x)$ is the blending weight.

Constraints on virtual views. To avoid overfitting during sparse view training, we generate unseen virtual views and

then apply the aforementioned regularization \mathcal{L}_{nc} and \mathcal{L}_d to these views. The virtual views are randomly generated as linear interpolations of a pair of training views’ poses, added with small perturbations. This way we have better consistency and smoother reconstructions of the shared area among training views.

3.2.2. Geometric Priors

To emphasize the geometric correctness of Gaussian splitting, we use the off-the-shelf monocular normal predictor, Metric3D [17], to provide additional geometric clues. Given the three input views, we feed them into Metric3D and get corresponding predicted normals $\hat{\mathbf{N}}$. Similar to [10], we directly apply L1 loss and cosine loss between rendered normal and predicted normal:

$$\mathcal{L}_{nr} = \sum_i \left(|\mathbf{N}_i - \hat{\mathbf{N}}_i| + \left(1 - \mathbf{N}_i \cdot \hat{\mathbf{N}}_i \right) \right). \quad (9)$$

Additionally, for the smoothness of the depth map, we apply the same normal loss to normal calculated depth map:

$$\mathcal{L}_{nd} = \sum_i \left(|\mathbf{n}_i - \hat{\mathbf{N}}_i| + \left(1 - \mathbf{n}_i \cdot \hat{\mathbf{N}}_i \right) \right). \quad (10)$$

3.3. Training

Initialization. Due to the sparsity of training input, a dense initialization can help speed up optimization. Therefore, we

Table 1. **Quantitative Comparison on DTU Dataset [20]**. We show the Chamfer Distance. Our SolidGS achieves the highest reconstruction accuracy among other methods. We also mark the best, second-best, and third-best results in red, orange, and yellow respectively.

Method	24	37	40	55	63	65	69	83	97	105	106	110	114	118	122	Mean
PGSR [7]	2.37	2.67	2.72	1.35	1.62	2.91	1.14	1.43	1.78	1.09	2.30	2.14	0.80	1.56	1.61	1.83
2DGS [18]	2.05	2.57	2.25	1.33	1.74	2.29	1.39	1.46	1.52	1.06	1.92	1.87	0.84	1.73	1.59	1.71
DNGaussian [23]	3.48	5.71	3.69	3.13	3.72	2.20	4.23	2.92	4.59	3.65	6.79	5.30	2.97	5.44	3.62	4.10
MVPGS [50]	1.93	2.31	1.99	1.07	1.44	2.97	1.31	1.37	1.23	1.04	1.85	1.02	0.83	1.54	1.33	1.55
SparseNeus [29]	4.81	5.56	5.81	2.68	3.30	3.88	2.39	2.91	3.08	2.33	2.64	3.12	1.74	3.55	2.31	3.34
NeuSurf [19]	1.35	3.25	2.50	0.80	1.21	2.35	0.77	1.19	1.20	1.05	1.05	1.21	0.41	0.80	1.08	1.35
SparseCraft [54]	2.29	2.67	2.99	0.69	1.43	2.18	1.16	1.30	1.52	1.14	1.86	-	0.56	1.00	1.12	1.57
Ours	1.50	2.40	2.20	0.98	0.88	1.36	0.79	1.29	1.33	1.06	1.72	1.07	0.60	0.99	0.89	1.27

Table 2. **Performance Comparison on DTU Dataset [20]**. PSNR is missing from SparseNeus [29] and NeuSurf [19] since they only reconstruct colorless meshes. Best results are highlighted in **bold**.

Method	Mean CD ↓	PSNR ↑	Training Time ↓
PGSR [7]	1.83	20.80	2.2min
2DGS [18]	1.71	20.65	2.1min
DNGaussian [23]	4.10	18.91	3.8min
MVPGS [50]	1.55	20.24	2.3min
SparseNeus [29]	3.34	-	>24h
NeuSurf [19]	1.35	-	>8h
SparseCraft [54]	1.57	20.55	10 min
Ours	1.27	21.32	3.1min

follow [50, 52] and leverage the MVSFormer [2] to generate 3D point clouds as initial positions of the Gaussians.

Loss function. The loss that we use to regularize the virtual views is:

$$\mathcal{L}_{virtual} = \lambda_d \mathcal{L}_d + \lambda_{nc} \mathcal{L}_{nc}, \quad (11)$$

and the total loss to train the input views is:

$$\mathcal{L} = \mathcal{L}_{virtual} + \mathcal{L}_c + \lambda_{nr} \mathcal{L}_{nr} + \lambda_{nd} \mathcal{L}_{nd} + \lambda_1 \mathcal{L}_s, \quad (12)$$

where \mathcal{L}_s is the flatten 3D Gaussian Loss used in PGSR [7] to form flattened Gaussians, and $\lambda_d = 10000$, $\lambda_{nc} = \lambda_{nr} = \lambda_{nd} = 0.015$, and $\lambda_1 = 100$ are preset constant weights. Since monocular normal estimation does not guarantee global consistency across the frame, we set the weights of two monocular normal guided losses λ_{nr} and λ_{nd} the same as the normal consistency loss λ_{nc} , hoping them to work at the same strength as regularization term and the RGB loss still dominants the training process.

Notice that we don’t put any constraints on the global solidness factor β_g during training. However, β_g tends to converge to maximize itself under our optimization, resulting in the Gaussian getting more solid.

Mesh extraction. We render the depth maps from the input views and then fuse them into a TSDF [9]. Then we extract the surface mesh using Marching Cube [30]. With highly consistent depth, we can extract a high-quality mesh with details from only 3 depth maps.

Table 3. **Quantitative Comparison on TNT Dataset [22]**. The best results are highlighted in **bold**.

Method	Barn	Truck	Caterpillar	Ignatius	Avg
PGSR [7]	0.06	0.09	0.02	0.13	0.08
2DGS [18]	0.20	0.27	0.12	0.25	0.21
MVPGS [50]	0.26	0.27	0.17	0.31	0.25
Ours	0.26	0.29	0.14	0.33	0.26

4. Experiments

4.1. Experiment Setup

Datasets. We conduct our experiments on three real-world datasets, DTU [20], Tanks and Temples(TNT) [22], and LLFF [31]. DTU dataset consists of 15 scenes of a single object with RGB images and depth scans. Foreground masks are used during evaluation following [34] and mesh extraction. TNT dataset contains large-scale indoor and outdoor scenes with intricate geometry. LLFF dataset contains RGB images of forward-facing scenes. We split the DTU and LLFF datasets following [19, 23, 34, 50] and split TNT with similar viewing angles variance in LLFF to train our method on 3 input images and test from unseen views.

Metrics. In DTU, we evaluate our mesh results by Chamfer Distance (CD) between reconstructed meshes and the fused ground-truth depth scans. We also report the PSNR in terms of NVS quality. In TNT, we report the precision of the reconstructed mesh. In LLFF, we visualize the mesh for visual comparison.

Baselines. We compare our SolidGS with representative reconstruction methods, which can be mainly categorized into three groups: 1. Gaussian-based explicit dense-view surface reconstruction methods, such as PGSR [7] and 2DGS [18]; 2. Gaussian-based explicit sparse-view NVS methods, such as DNGaussian [23] and MVPGS [50]; and 3. neural implicit sparse-view surface reconstruction methods, such as SparseNeus [29], NeuSurf [19], and SparseCraft [54]. For a fair comparison, we use the same point clouds from NVSFormer [2] as initialization in PGSR and 2DGS.

Implementation Details. Our method is built upon the public code of PGSR [7] with our modified CUDA ker-

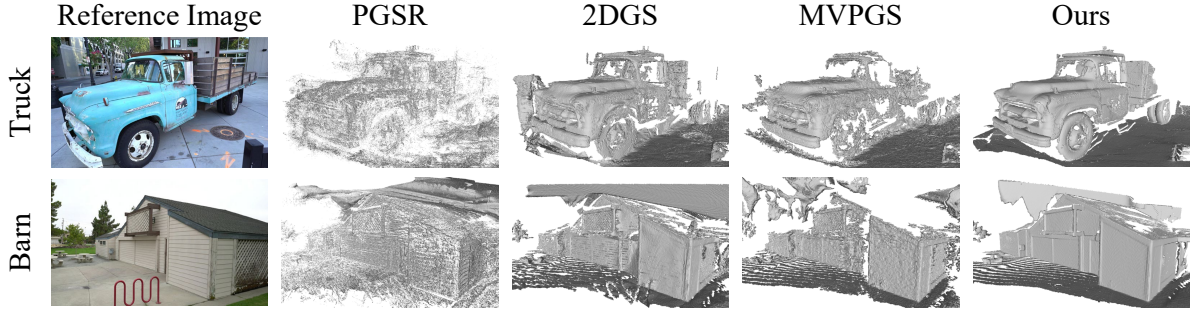


Figure 5. **Qualitative Mesh Results on TNT Dataset.** All meshes are extracted using TSDF + Marching Cube from Gaussians.

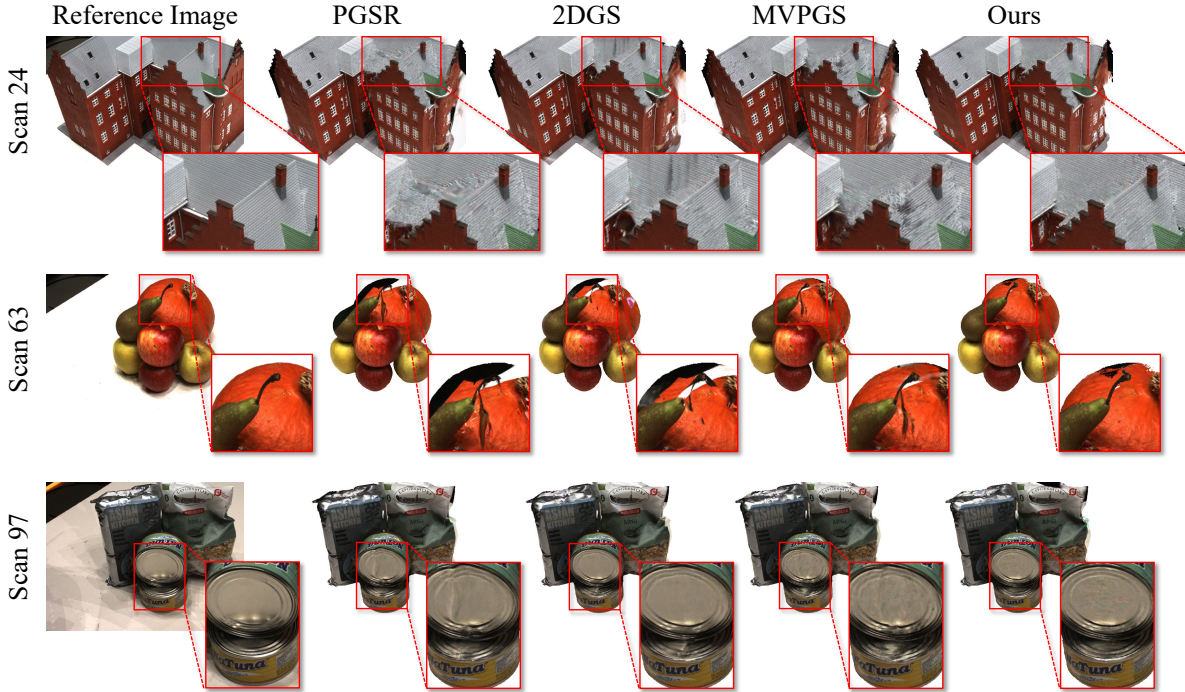


Figure 6. **Qualitative NVS Results on DTU Dataset.** We demonstrate novel view synthesis results of our method against PGSR [7], 2DGS [23], and MVPGS [50]. Backgrounds are masked out in all inference images.

nels so that it can take in shared solidity factor and other geometric regularization. We incorporate default training parameters and the densification strategy in 3DGS, except that we change the total iterations to 10000 and the densification stops at 5000 iterations. Geometric regularization is involved in the training starting at 1000 iterations. During training, we reset the solidity factor every 1000 iterations in the first 5000 iterations. Virtual cameras are used every 50 iterations. We conducted all our experiments on a desktop with an i9-13900K CPU and an RTX 4090 GPU.

4.2. Surface Reconstruction Results

In Tab. 1 and Tab. 2, we compare our surface reconstruction to the baselines we selected on Chamfer Distance and training time on the DTU dataset. Our method achieves

the highest geometry reconstruction quality with the least CD among all compared methods. Compared to the dense view methods 2DGS [18] and PGSR [7], our method significantly enhances the surface quality in each scan with little training time overhead. Compared to implicit methods SparseNeus [29], NeuSurf [19], and SparseCraft [54], our method benefits from the fast rendering of Gaussian Splatting and trains significantly faster with better geometry.

Fig. 4 provides the qualitative comparison of the reconstructed mesh. Among all explicit methods, our mesh achieves the highest quality in terms of geometry accuracy, completeness, and detail sharpness. Compared to the PGSR and 2DGS, our method captures better details due to the geometry priors. Due to our SolidGS, the depths are precise and consistent across views, which gives fewer floating

Table 4. **Quantitative Ablation Study on DTU dataset [20].**

Setting	Accuracy ↓	Completion ↓	Average ↓
Base	1.76	1.91	1.83
Base + Regularization	1.50	1.76	1.63
Base + SolidGS	1.43	1.72	1.58
Base + Mono Normal	1.18	1.54	1.36
Full	1.09	1.45	1.27

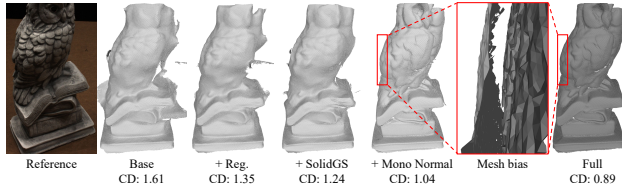


Figure 7. **Qualitative ablation on DTU.** We simultaneously visualize the mesh of ”+ Mono Normal” and ”Full” inside the red box.

artifacts and faithful geometry to ground truth. MVPGS renders highly inconsistent depth maps and reconstructs broken meshes. The Chamfer Distance doesn’t reflect the mesh completeness, therefore, MVPGS have the lowest CD in some scenes. Mesh completeness is more obviously demonstrated in Fig. 4. In comparison with the neural implicit method NeuSurf, our method reconstructs the sharper edges and cutoffs between objects.

We demonstrate our method’s capability in reconstructing large-scale scenes from sparse input in Tab. 3 and Fig. 5. PGSR [7] cannot converge to a consistent geometry across multiple input views, resulting in a broken mesh and low precision scores. Our method reaches the highest average precision compared to 2DGS [18] and MVPGS [50]. Our method is superior in mesh completeness and correctness notably from the visual results.

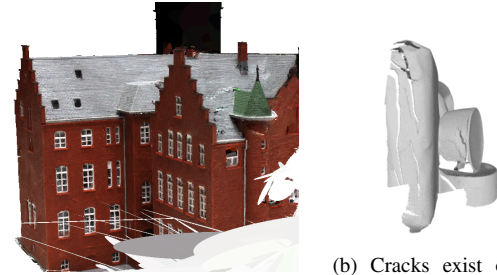
More results including the LLFF dataset can be found in the Supplementary.

4.3. Novel View Synthesis Results

Our approach models scenes as a radiance field, enabling the rendering of high-quality images from new perspectives. We compare our Novel View Synthesis (NVS) results against all baselines in Tab. 1. With the correct geometry, our method has fewer artifacts in the final Gaussian field and reaches the highest PSNR in the NVS task. A qualitative comparison is performed in Fig. 6. For the roof in scan 24, the pumpkin in scan 63, and the cans in scan 97, there all exist visual artifacts due to geometry mismatches in the baselines. Our method reconstructs geometry that is plausible from novel views, greatly improving the NVS results.

4.4. Ablations

We conduct our ablation study on the DTU dataset (Tab. 4 and Fig. 7). Starting from our baseline PGSR [7], we first show the effect of additional geometric regularizations, including virtual camera and depth distortion loss. This mod-



(a) Renderings with large viewpoint change. (b) Cracks exist on regions visible to one view.

Figure 8. **Limitations.** Artifacts occur with novel views.

ification gives us a smoother geometry over limited training views, which is reflected by a less erroneous shape on the fused mesh. Then we show the effect of our modified SolidGS. Compared to the based model, this modification makes Gaussian closer to solid surfels during training, thus leading to a more accurate depth blending and fewer floater artifacts in the fused mesh. Third, by introducing monocular normal prior, we have a mesh that is self-consistent in shape. Notice that when we compare this modification against the full model, there is a huge bias between the two meshes, which leads to a higher Chamfer distance. That’s because our SolidGS gives high accuracy and uniform geometry during training, and therefore mitigates the depth inconsistency caused by the inaccurate geometry rendering. Putting every component together, our method reconstructs a smooth, precise, and complete mesh.

4.5. Limitations and Future Works

Although our method achieves great progress in extracting a mesh from overlapping areas from sparse view inputs, our method can be unstable in areas that appear in only one training view. This is reflected by the cracks on the edge of the mesh, as shown in Fig. 8b and the rendering quality could largely decrease with the deviation of rendering viewpoints from the input sparse view as shown in Fig. 8a. To mitigate this limitation, it is worth investigating identifying local geometry connectivity from training views and enforcing this connectivity during training. We leave all the above exploration for future works.

5. Conclusion

In conclusion, we present SolidGS, a method for enhancing sparse-view surface reconstruction through consolidated Gaussian splatting. By introducing SolidGS with a global learnable solidness factor, our approach promotes multi-view geometry consistency, leading to high-fidelity reconstructions even with limited input views. The integration of geometric regularizations and priors further supports stable optimization, allowing SolidGS to produce detailed and precise meshes within minutes. Experiments show that our methods achieve state-of-the-art in both surface reconstruction and novel view synthesis from sparse inputs.

References

- [1] Zhenyu Bao, Guibiao Liao, Kaichen Zhou, Kanglin Liu, Qing Li, and Guoping Qiu. Loopsparsegs: Loop based sparse-view friendly gaussian splatting. *arXiv preprint arXiv:2408.00254*, 2024. 3
- [2] Chenjie Cao, Xinlin Ren, and Yanwei Fu. Mvsformer: Learning robust image representations via transformers and temperature-based depth for multi-view stereo. *arXiv preprint arXiv:2208.02541*, 5, 2022. 6
- [3] Eric R Chan, Connor Z Lin, Matthew A Chan, Koki Nagano, Boxiao Pan, Shalini De Mello, Orazio Gallo, Leonidas J Guibas, Jonathan Tremblay, Sameh Khamis, et al. Efficient geometry-aware 3d generative adversarial networks. In *Proceedings of the IEEE/CVF conference on computer vision and pattern recognition*, pages 16123–16133, 2022. 3
- [4] David Charatan, Sizhe Lester Li, Andrea Tagliasacchi, and Vincent Sitzmann. pixelsplat: 3d gaussian splats from image pairs for scalable generalizable 3d reconstruction. In *Proceedings of the IEEE/CVF Conference on Computer Vision and Pattern Recognition*, pages 19457–19467, 2024. 3
- [5] Anpei Chen, Zexiang Xu, Fuqiang Zhao, Xiaoshuai Zhang, Fanbo Xiang, Jingyi Yu, and Hao Su. Mvsnerf: Fast generalizable radiance field reconstruction from multi-view stereo. In *Proceedings of the IEEE/CVF international conference on computer vision*, pages 14124–14133, 2021. 3
- [6] Anpei Chen, Zexiang Xu, Andreas Geiger, Jingyi Yu, and Hao Su. Tensorf: Tensorial radiance fields. In *European conference on computer vision*, pages 333–350. Springer, 2022. 3
- [7] Danpeng Chen, Hai Li, Weicai Ye, Yifan Wang, Weijian Xie, Shangjin Zhai, Nan Wang, Haomin Liu, Hujun Bao, and Guofeng Zhang. Pgsr: Planar-based gaussian splatting for efficient and high-fidelity surface reconstruction. *arXiv preprint arXiv:2406.06521*, 2024. 1, 2, 3, 4, 5, 6, 7, 8
- [8] Yuedong Chen, Haoifei Xu, Chuanxia Zheng, Bohan Zhuang, Marc Pollefeys, Andreas Geiger, Tat-Jen Cham, and Jianfei Cai. Mvsplat: Efficient 3d gaussian splatting from sparse multi-view images. In *European Conference on Computer Vision*, pages 370–386. Springer, 2025. 3
- [9] Brian Curless and Marc Levoy. A volumetric method for building complex models from range images. In *Proceedings of the 23rd annual conference on Computer graphics and interactive techniques*, pages 303–312, 1996. 6
- [10] Pinxuan Dai, Jiamin Xu, Wenxiang Xie, Xinguo Liu, Huamin Wang, and Weiwei Xu. High-quality surface reconstruction using gaussian surfels. In *ACM SIGGRAPH 2024 Conference Papers*, pages 1–11, 2024. 5
- [11] Kangle Deng, Andrew Liu, Jun-Yan Zhu, and Deva Ramanan. Depth-supervised nerf: Fewer views and faster training for free. In *Proceedings of the IEEE/CVF Conference on Computer Vision and Pattern Recognition*, pages 12882–12891, 2022. 3
- [12] Yilun Du, Cameron Smith, Ayush Tewari, and Vincent Sitzmann. Learning to render novel views from wide-baseline stereo pairs. In *Proceedings of the IEEE/CVF Conference on Computer Vision and Pattern Recognition*, pages 4970–4980, 2023. 3
- [13] Sara Fridovich-Keil, Alex Yu, Matthew Tancik, Qinhong Chen, Benjamin Recht, and Angjoo Kanazawa. Plenoxels: Radiance fields without neural networks. In *Proceedings of the IEEE/CVF conference on computer vision and pattern recognition*, pages 5501–5510, 2022. 3
- [14] Qiancheng Fu, Qingshan Xu, Yew Soon Ong, and Wenbing Tao. Geo-neus: Geometry-consistent neural implicit surfaces learning for multi-view reconstruction. *Advances in Neural Information Processing Systems*, 35:3403–3416, 2022. 3
- [15] Antoine Guédon and Vincent Lepetit. Sugar: Surface-aligned gaussian splatting for efficient 3d mesh reconstruction and high-quality mesh rendering. In *Proceedings of the IEEE/CVF Conference on Computer Vision and Pattern Recognition*, pages 5354–5363, 2024. 3
- [16] Abdullah Hamdi, Luke Melas-Kyriazi, Jinjie Mai, Guocheng Qian, Ruoshi Liu, Carl Vondrick, Bernard Ghanem, and Andrea Vedaldi. Ges: Generalized exponential splatting for efficient radiance field rendering. In *Proceedings of the IEEE/CVF Conference on Computer Vision and Pattern Recognition*, pages 19812–19822, 2024. 2, 4
- [17] Mu Hu, Wei Yin, Chi Zhang, Zhipeng Cai, Xiaoxiao Long, Hao Chen, Kaixuan Wang, Gang Yu, Chunhua Shen, and Shaojie Shen. Metric3d v2: A versatile monocular geometric foundation model for zero-shot metric depth and surface normal estimation. *arXiv preprint arXiv:2404.15506*, 2024. 2, 5
- [18] Binbin Huang, Zehao Yu, Anpei Chen, Andreas Geiger, and Shenghua Gao. 2d gaussian splatting for geometrically accurate radiance fields. In *ACM SIGGRAPH 2024 Conference Papers*, pages 1–11, 2024. 1, 2, 3, 5, 6, 7, 8
- [19] Han Huang, Yulun Wu, Junsheng Zhou, Ge Gao, Ming Gu, and Yu-Shen Liu. Neusurf: On-surface priors for neural surface reconstruction from sparse input views. In *Proceedings of the AAAI Conference on Artificial Intelligence*, pages 2312–2320, 2024. 2, 3, 5, 6, 7
- [20] Rasmus Jensen, Anders Dahl, George Vogiatzis, Engin Tola, and Henrik Aanæs. Large scale multi-view stereopsis evaluation. In *Proceedings of the IEEE conference on computer vision and pattern recognition*, pages 406–413, 2014. 2, 6, 8, 3
- [21] Bernhard Kerbl, Georgios Kopanas, Thomas Leimkühler, and George Drettakis. 3d gaussian splatting for real-time radiance field rendering. *ACM Trans. Graph.*, 42(4):139–1, 2023. 1, 3, 4
- [22] Arno Knapitsch, Jaesik Park, Qian-Yi Zhou, and Vladlen Koltun. Tanks and temples: Benchmarking large-scale scene reconstruction. *ACM Transactions on Graphics (ToG)*, 36(4):1–13, 2017. 2, 6, 1
- [23] Jiahe Li, Jiawei Zhang, Xiao Bai, Jin Zheng, Xin Ning, Jun Zhou, and Lin Gu. Dngaussian: Optimizing sparse-view 3d gaussian radiance fields with global-local depth normalization. In *Proceedings of the IEEE/CVF Conference on Computer Vision and Pattern Recognition*, pages 20775–20785, 2024. 2, 3, 6, 7
- [24] Zhaoshuo Li, Thomas Müller, Alex Evans, Russell H Taylor, Mathias Unberath, Ming-Yu Liu, and Chen-Hsuan Lin. Neuralangelo: High-fidelity neural surface reconstruction. In

- Proceedings of the IEEE/CVF Conference on Computer Vision and Pattern Recognition*, pages 8456–8465, 2023. 1
- [25] Zhihao Liang, Zhangjin Huang, Changxing Ding, and Kui Jia. Helixsurf: A robust and efficient neural implicit surface learning of indoor scenes with iterative intertwined regularization. In *Proceedings of the IEEE/CVF Conference on Computer Vision and Pattern Recognition*, pages 13165–13174, 2023. 3
- [26] Zhihao Liang, Qi Zhang, Wenbo Hu, Ying Feng, Lei Zhu, and Kui Jia. Analytic-splatting: Anti-aliased 3d gaussian splatting via analytic integration. *arXiv preprint arXiv:2403.11056*, 2024. 3
- [27] Shichen Liu, Tianye Li, Weikai Chen, and Hao Li. Soft rasterizer: A differentiable renderer for image-based 3d reasoning. In *Proceedings of the IEEE/CVF international conference on computer vision*, pages 7708–7717, 2019. 2
- [28] Stephen Lombardi, Tomas Simon, Jason Saragih, Gabriel Schwartz, Andreas Lehrmann, and Yaser Sheikh. Neural volumes: Learning dynamic renderable volumes from images. *arXiv preprint arXiv:1906.07751*, 2019. 3
- [29] Xiaoxiao Long, Cheng Lin, Peng Wang, Taku Komura, and Wenping Wang. Sparseneus: Fast generalizable neural surface reconstruction from sparse views. In *European Conference on Computer Vision*, pages 210–227. Springer, 2022. 2, 3, 6, 7
- [30] William E Lorensen and Harvey E Cline. Marching cubes: A high resolution 3d surface construction algorithm. In *Seminal graphics: pioneering efforts that shaped the field*, pages 347–353. 1998. 6
- [31] Ben Mildenhall, Pratul P Srinivasan, Rodrigo Ortiz-Cayon, Nima Khademi Kalantari, Ravi Ramamoorthi, Ren Ng, and Abhishek Kar. Local light field fusion: Practical view synthesis with prescriptive sampling guidelines. *ACM Transactions on Graphics (ToG)*, 38(4):1–14, 2019. 2, 6, 1
- [32] Ben Mildenhall, Pratul P Srinivasan, Matthew Tancik, Jonathan T Barron, Ravi Ramamoorthi, and Ren Ng. Nerf: Representing scenes as neural radiance fields for view synthesis. *Communications of the ACM*, 65(1):99–106, 2021. 1, 3
- [33] Thomas Müller, Alex Evans, Christoph Schied, and Alexander Keller. Instant neural graphics primitives with a multi-resolution hash encoding. *ACM transactions on graphics (TOG)*, 41(4):1–15, 2022. 3
- [34] Michael Niemeyer, Jonathan T Barron, Ben Mildenhall, Mehdi SM Sajjadi, Andreas Geiger, and Noha Radwan. Regnerf: Regularizing neural radiance fields for view synthesis from sparse inputs. In *Proceedings of the IEEE/CVF Conference on Computer Vision and Pattern Recognition*, pages 5480–5490, 2022. 3, 6
- [35] Avinash Paliwal, Wei Ye, Jinhui Xiong, Dmytro Kotovenko, Rakesh Ranjan, Vikas Chandra, and Nima Khademi Kalantari. Coherentgs: Sparse novel view synthesis with coherent 3d gaussians. In *European Conference on Computer Vision*, pages 19–37. Springer, 2025. 3
- [36] Haoxuan Qu, Zhuoling Li, Hossein Rahmani, Yujun Cai, and Jun Liu. Disc-gs: Discontinuity-aware gaussian splatting. *arXiv preprint arXiv:2405.15196*, 2024. 3
- [37] Nikhila Ravi, Jeremy Reizenstein, David Novotny, Taylor Gordon, Wan-Yen Lo, Justin Johnson, and Georgia Gkioxari. Accelerating 3d deep learning with pytorch3d. *arXiv preprint arXiv:2007.08501*, 2020. 2
- [38] Yufan Ren, Fangjinhua Wang, Tong Zhang, Marc Pollefeys, and Sabine Süsstrunk. Volrecon: Volume rendering of signed ray distance functions for generalizable multi-view reconstruction. In *Proceedings of the IEEE/CVF Conference on Computer Vision and Pattern Recognition*, pages 16685–16695, 2023. 3
- [39] Barbara Roessle, Jonathan T Barron, Ben Mildenhall, Pratul P Srinivasan, and Matthias Nießner. Dense depth priors for neural radiance fields from sparse input views. In *Proceedings of the IEEE/CVF Conference on Computer Vision and Pattern Recognition*, pages 12892–12901, 2022. 3
- [40] Johannes Lutz Schönberger, Enliang Zheng, Marc Pollefeys, and Jan-Michael Frahm. Pixelwise view selection for unstructured multi-view stereo. In *European Conference on Computer Vision (ECCV)*, 2016. 1
- [41] Nagabhushan Somraj and Rajiv Soundararajan. Vip-nerf: Visibility prior for sparse input neural radiance fields. In *ACM SIGGRAPH 2023 Conference Proceedings*, pages 1–11, 2023. 3
- [42] Mohammed Suhail, Carlos Esteves, Leonid Sigal, and Ameesh Makadia. Generalizable patch-based neural rendering. In *European Conference on Computer Vision*, pages 156–174. Springer, 2022. 3
- [43] Cheng Sun, Min Sun, and Hwann-Tzong Chen. Direct voxel grid optimization: Super-fast convergence for radiance fields reconstruction. In *Proceedings of the IEEE/CVF conference on computer vision and pattern recognition*, pages 5459–5469, 2022. 3
- [44] Guangcong Wang, Zhaoxi Chen, Chen Change Loy, and Ziwei Liu. Sparsenerf: Distilling depth ranking for few-shot novel view synthesis. In *Proceedings of the IEEE/CVF International Conference on Computer Vision*, pages 9065–9076, 2023. 3
- [45] Jiepeng Wang, Peng Wang, Xiaoxiao Long, Christian Theobalt, Taku Komura, Lingjie Liu, and Wenping Wang. Neuris: Neural reconstruction of indoor scenes using normal priors. In *European Conference on Computer Vision*, pages 139–155. Springer, 2022. 3
- [46] Peng Wang, Lingjie Liu, Yuan Liu, Christian Theobalt, Taku Komura, and Wenping Wang. Neus: Learning neural implicit surfaces by volume rendering for multi-view reconstruction. *arXiv preprint arXiv:2106.10689*, 2021. 1, 3
- [47] Haoyu Wu, Alexandros Graikos, and Dimitris Samaras. S-volsdf: Sparse multi-view stereo regularization of neural implicit surfaces. In *Proceedings of the IEEE/CVF International Conference on Computer Vision*, pages 3556–3568, 2023. 3
- [48] Haolin Xiong, Sairisheek Muttukuru, Rishi Upadhyay, Pradyumna Chari, and Achuta Kadambi. Sparsegs: Real-time 360 {deg} sparse view synthesis using gaussian splatting. *arXiv preprint arXiv:2312.00206*, 2023. 3
- [49] Qiangeng Xu, Zexiang Xu, Julien Philip, Sai Bi, Zhixin Shu, Kalyan Sunkavalli, and Ulrich Neumann. Pointnerf: Point-based neural radiance fields. In *Proceedings of*

- the IEEE/CVF conference on computer vision and pattern recognition*, pages 5438–5448, 2022. [3](#)
- [50] Wangze Xu, Huachen Gao, Shihe Shen, Rui Peng, Jianbo Jiao, and Ronggang Wang. Mvpgs: Excavating multi-view priors for gaussian splatting from sparse input views. *arXiv preprint arXiv:2409.14316*, 2024. [1](#), [2](#), [3](#), [5](#), [6](#), [7](#), [8](#)
- [51] Jiawei Yang, Marco Pavone, and Yue Wang. Freenerf: Improving few-shot neural rendering with free frequency regularization. In *Proceedings of the IEEE/CVF conference on computer vision and pattern recognition*, pages 8254–8263, 2023. [3](#)
- [52] Yao Yao, Zixin Luo, Shiwei Li, Tian Fang, and Long Quan. Mvsnet: Depth inference for unstructured multi-view stereo. In *Proceedings of the European conference on computer vision (ECCV)*, pages 767–783, 2018. [6](#)
- [53] Lior Yariv, Jiatao Gu, Yoni Kasten, and Yaron Lipman. Volume rendering of neural implicit surfaces. *Advances in Neural Information Processing Systems*, 34:4805–4815, 2021. [1](#), [3](#)
- [54] Mae Younes, Amine Ouasfi, and Adnane Boukhayma. Sparsecraft: Few-shot neural reconstruction through stereopsis guided geometric linearization. *arXiv preprint arXiv:2407.14257*, 2024. [3](#), [6](#), [7](#)
- [55] Alex Yu, Vickie Ye, Matthew Tancik, and Angjoo Kanazawa. pixelnerf: Neural radiance fields from one or few images. In *Proceedings of the IEEE/CVF conference on computer vision and pattern recognition*, pages 4578–4587, 2021. [3](#)
- [56] Ruihan Yu, Tianyu Huang, Jingwang Ling, and Feng Xu. 2dgh: 2d gaussian-hermite splatting for high-quality rendering and better geometry reconstruction. *arXiv preprint arXiv:2408.16982*, 2024. [1](#)
- [57] Zehao Yu, Anpei Chen, Binbin Huang, Torsten Sattler, and Andreas Geiger. Mip-splatting: Alias-free 3d gaussian splatting. In *Proceedings of the IEEE/CVF Conference on Computer Vision and Pattern Recognition*, pages 19447–19456, 2024. [3](#)
- [58] Zehao Yu, Torsten Sattler, and Andreas Geiger. Gaussian opacity fields: Efficient and compact surface reconstruction in unbounded scenes. *arXiv preprint arXiv:2404.10772*, 2024. [1](#), [3](#), [5](#)
- [59] Weixing Zhang, Zongrui Li, De Ma, Huajin Tang, Xudong Jiang, Qian Zheng, and Gang Pan. Spiking gs: Towards high-accuracy and low-cost surface reconstruction via spiking neuron-based gaussian splatting. *arXiv preprint arXiv:2410.07266*, 2024. [1](#)
- [60] Zehao Zhu, Zhiwen Fan, Yifan Jiang, and Zhangyang Wang. Fsgs: Real-time few-shot view synthesis using gaussian splatting. In *European Conference on Computer Vision*, pages 145–163. Springer, 2025. [3](#)

SolidGS: Consolidating Gaussian Surfel Splatting for Sparse-View Surface Reconstruction

Supplementary Material

6. Summary

This supplementary includes a **video** demonstrating the qualitative results of geometry reconstruction and Novel View Synthesis. We also showcase more results on DTU, Tanks-and-Temples, and LLFF datasets. We compare the effect of training view number. We also include a discussion on the concurrent works.

7. More results

7.1. Results on Tanks-and-Temples Dataset

In Fig. 9 we provide more qualitative comparisons of our method against all explicit reconstruction techniques on the Tanks-and-Temples (TNT) dataset [22]. In the Caterpillar and Ignatius scenes, our method reconstructs surfaces with higher completeness of the centroid structure.

7.2. Results on LLFF Dataset

In Fig. 10 we present a qualitative comparison of our method against all explicit reconstruction techniques on the LLFF dataset [31]. In the Room scene, our approach effectively reconstructs the walls and tables, whereas other methods exhibit distorted geometry and contain holes. In the Fortress scene, our method accurately captures the shape of the fortress with reduced noise on the mesh. Additionally, our method produces a flatter and more complete table in the reconstructed surface.

7.3. Different Input Views

Tab. 5 presents the quantitative results for various input views on the DTU Dataset. Our method consistently achieves the highest Completion and Chamfer Distance across all settings, indicating its robustness with different training views. Additionally, as the number of training views increases, our method’s accuracy improves more rapidly compared to MVPGS. This highlights its greater potential from additional training views.

Fig. 11 displays our qualitative results with six input views, demonstrating that increased input views enhance reconstruction quality with finer details. We also present our qualitative results of reconstructed mesh in Fig. 12. Even with extremely sparse input (2 views), our method still reconstructs plausible results, surpassing all other methods.

8. Discussion on Concurrent Works

We observe that concurrent works such as SpikingGS [59] and 2DGH [56] have modified Gaussian kernel functions

in Gaussian splatting to enhance geometric reconstruction accuracy. SpikingGS [59] employs spiking neurons on the opacity of Gaussians and their kernel functions, effectively eliminating semi-transparent Gaussians and their tails. Although our motivations align, our approach, SolidGS, reconstructs a more continuous volume representation, resulting in superior novel view quality. Conversely, 2DGH [56] replaces the traditional Gaussian kernel with a Gaussian-Hermite kernel to augment the expressiveness of individual Gaussians. However, this method introduces increased ambiguity, particularly in under-supervised regions. Our SolidGS focuses on consolidating opacity during rendering, thereby mitigating multiview geometry inconsistencies. Additionally, SolidGS incorporates more geometric constraints to achieve high-fidelity surface reconstruction, even under challenging sparse input conditions.

Table 5. **Quantitative Comparison on DTU Dataset [20] with Different Input Views.** We show the Accuracy (Accu.), Completion (Comp), and Chamfer Distance (CD). We mark the best and second-best results in red and orange respectively.

Methods	2 view			3 view			4 view			5 view			6 view		
	Accu. ↓	Comp. ↓	CD ↓	Accu. ↓	Comp. ↓	CD ↓	Accu. ↓	Comp. ↓	CD ↓	Accu. ↓	Comp. ↓	CD ↓	Accu. ↓	Comp. ↓	CD ↓
PGSR	2.02	2.50	2.26	1.76	1.91	1.83	1.46	1.55	1.51	1.10	1.26	1.18	0.84	0.98	0.91
2DGS	1.84	2.16	2.00	1.54	1.88	1.71	1.45	1.74	1.59	1.32	1.64	1.48	1.10	1.46	1.28
MVPGS	1.02	2.87	1.94	1.09	2.01	1.55	0.95	1.55	1.25	0.81	1.35	1.08	0.73	1.15	0.94
Ours	1.27	1.95	1.61	1.09	1.45	1.27	1.01	1.26	1.13	0.80	0.97	0.89	0.66	0.83	0.75

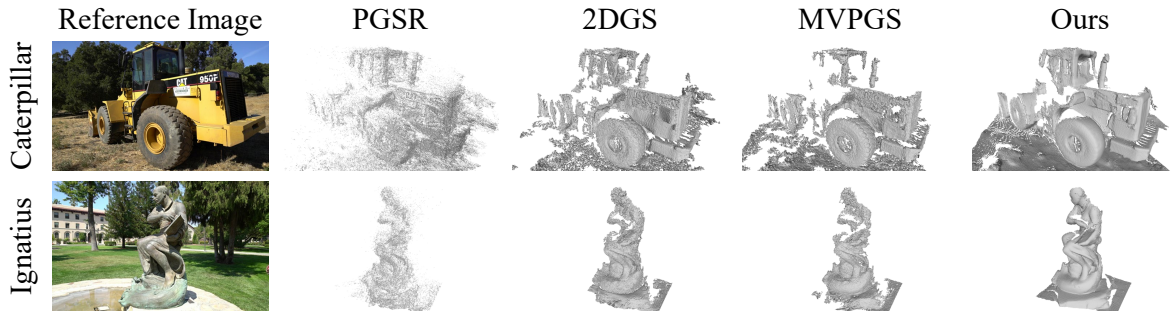


Figure 9. **Qualitative Mesh Results on TNT Dataset [22].** All meshes are extracted using TSDF + Marching Cube from Gaussians.

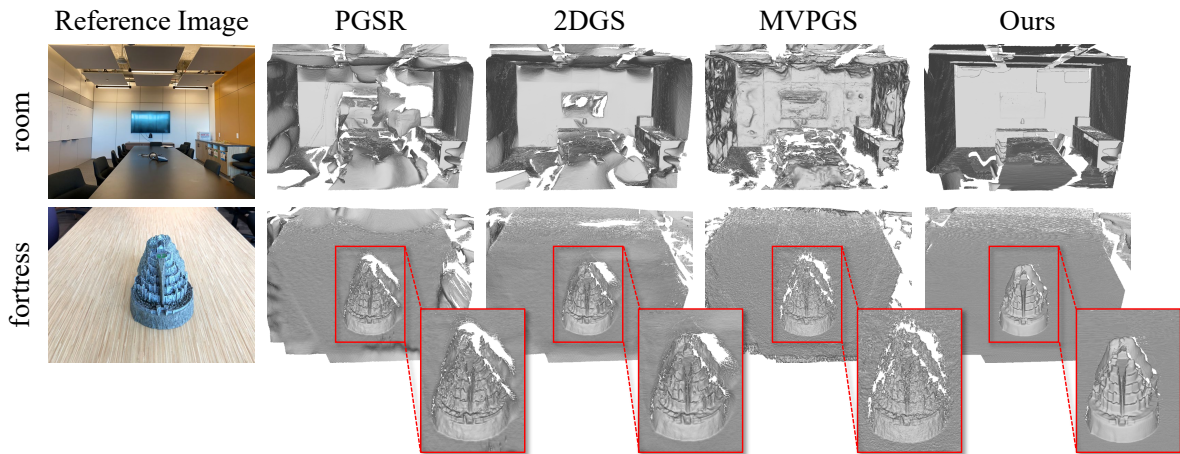


Figure 10. **Qualitative Mesh Results on LLFF Dataset [31].** All meshes are extracted using TSDF + Marching Cube from Gaussians.

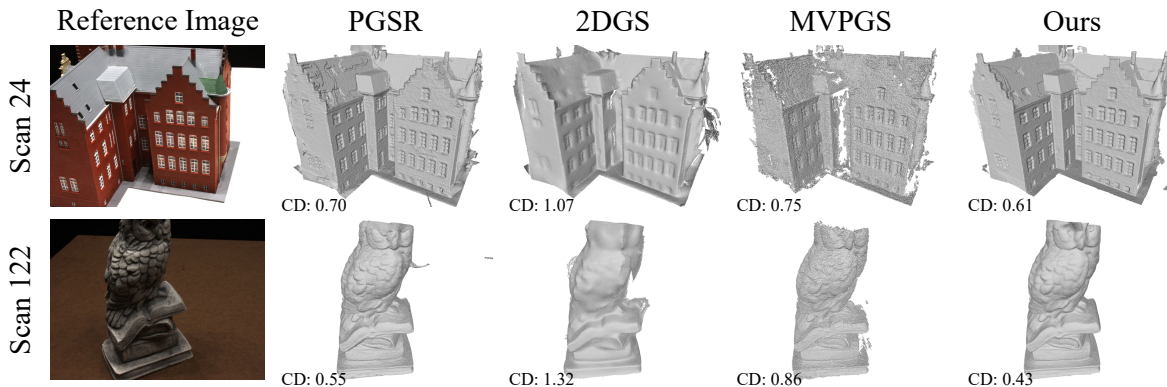


Figure 11. **Qualitative Mesh Results on DTU Dataset [20] with 6 Input Views.**

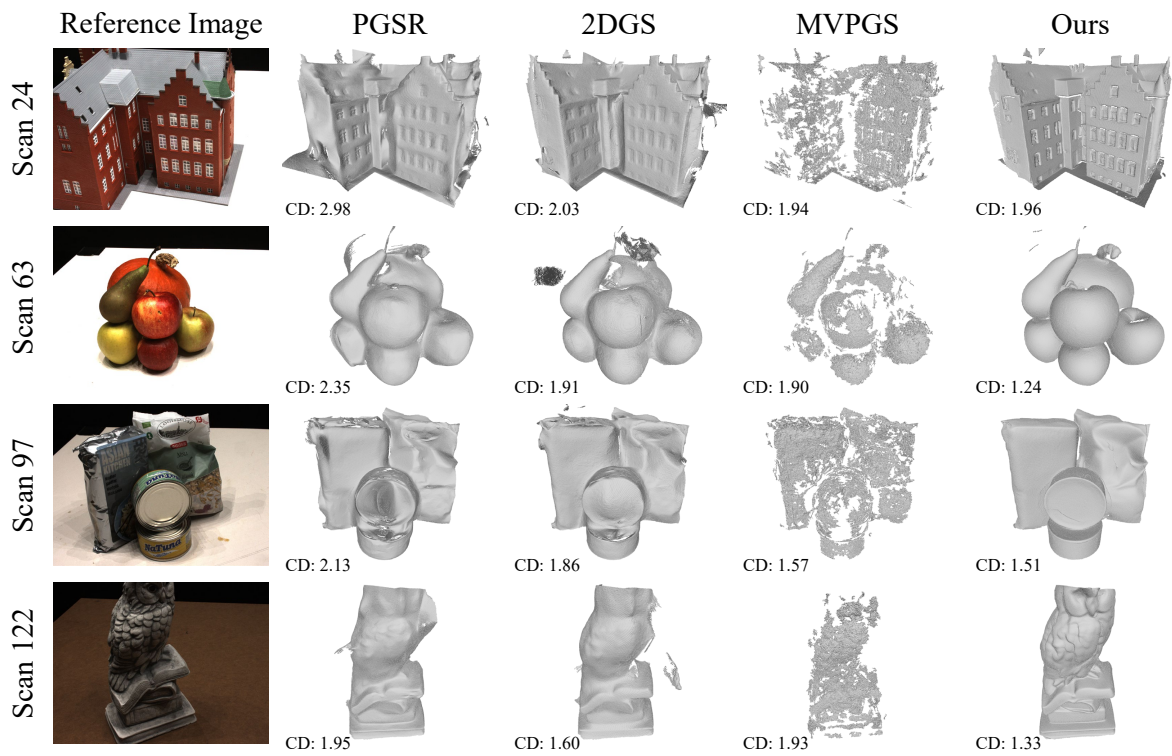


Figure 12. Qualitative Mesh Results on DTU Dataset [20] with 2 Input Views.